https://doi.org/10.1016/j.apacoust.2020.107633

Hybrid microphone array signal processing approach for faulty wheel identification and ground impedance estimation in wheel/rail system

Long Chen[1], Yat-Sze Choy*[1], Kai-Chung Tam[2], Cheng-Wei Fei[3]
[1] Department of Mechanical Engineering, The Hong Kong Polytechnic University. 11 Yuk Choi Rd, 999077, Hong Kong
[2] Kinetics Noise Control (ASIA) LTD., Unit E, 9/F., World Tech Centre, 95 How Ming Street, Kwun Tong, Hong Kong
[3] Department of Aeronautics and Astronautics, Fudan University, Shanghai 200433, China
*Corresponding author.
E-mail address: mmyschoy@polyu.edu.hk

Abstract

This study investigates a microphone array signal processing approach in a theoretical and experimental manner for faulty wheel identification and localisation and ground impedance estimation in a wheel/rail system. The sound source location during wheel rotation is estimated by a broadband weighted multiple signal classification (BW-MUSIC) method, while the impedance of the corresponding ground surface is estimated by the Levenberg–Marquardt and Crank Nicolson (LM–CN) method. The accurate location of the faulty wheel is determined by the kurtosis beamformer. As an acoustics-based noncontact diagnosis method, this technique overcomes the challenge presented by contact between the sensors and the examined structures, and it is more applicable for impulsive signals with broadband features, such as impact noise generated from faults on the wheel surface. The accuracy of the location and impedance estimations is also examined in this study, and the results obtained from the numerical and experimental analyses are observed to be in good agreement. With multiple sound sources and the interference of ground reflection, the BW-MUSIC method can provide a separate and distinct localisation result in the sound map, while the LM–CN method can provide a

preferable estimation result of the ground impedance, allowing the faulty wheel to be detected accurately.

Keywords: array signal processing; ground impedance; beamforming; impulsive signal;

1. Introduction

In a wheel/rail system, the wheels and rail are prone to wear out or become damaged due to their frequent operation, leading to an uneven surface or an irregular shape. Nearly half of the train accidents were the result of the wheel-set faults in the wheel/rail system, and the comprehensive maintenance cost of the wheels can be expensive. When the wheels pass over the rail, a rolling noise is generated. This is caused predominantly by the undulations of the wheel and the surface of the rail that induce a related vertical vibration. Impact noise is also generated when the wheels pass over the uneven structural surfaces of the rail [1] It is hard for engineers to identify the location of the faults accurately by visual checking or hearing. Generally, impact noise has an impulsive signal feature that is a sharp, short duration pulse with a peak amplitude much higher than that of rolling noise. Moreover, it occurs in a periodic pattern according to the cycle of a rotating faulty wheel, with broadband, short duration, low acoustic energy level, low signal-to-noise ratio (SNR), and quasi-periodical nonstationary characteristics [2]. One should not neglect the fact that the uneven structure of the wheels or rail has the potential to cause an accident, apart from the aspect that the noise is an annoyance. In matters of safety, maintenance is essential [3]. However, comprehensive maintenance such as checking all the wheels of a train would be very expensive. To solve this problem, wheel/rail systems require a reliable structural condition monitoring system.

Over the past few decades, a variety of fault detection methods have been developed, such as vibration analysis, magnetic testing, Lamb wave analysis, and acoustic emission (AE) [4-10]. However, these fault detection approaches can mostly be regarded as contact methods, as the sensors are required to be mounted on the surface of the structure with wiring. This causes problems with placement of wiring on the rotating structure, and inaccurate measuring results due to an additional loading on the light structure. In this regard, non-contact measurement approaches, such as acoustics-based diagnosis (ABD), may provide valid alternatives. For example, Shibata et al. utilised the symmetrised dot pattern (SDP) method to detect abnormalities in bearings, and Lu et al. used the near-field acoustical holography (NAH) technique to detect faults in a gear box [11, 12]. Recently, Cabada et al. used spectrum kurtosis (SK) beamforming to detect the faulty pinion in the rotating machinery test rig in the frequency domain [13]. Chen et al. introduced a time-domain kurtosis beamformer to effectively locate and identify the different kinds of structural faults of the wheels against a moderately high background noise [14]. Different types of faults including a dent with the depth of 0.2 mm on the wheel surface is considered in this research. The relevant studies showed that the kurtosis indicator can effectively reflect the signal impulsiveness for the fault detection, outperforming the traditional beamforming power and peak value [15, 16]. Furthermore, the time-domain kurtosis beamformer is more straightforward and effective than the frequency-domain method to indicate the impact acoustics signal with broadband features because it is difficult to choose a suitable frequency band.

However, the beamforming map of the fault proposed by Chen et al. is based on the free field assumption. In reality, ground with different material properties exists underneath the rail. Due to the ground reflection, there is image sound sources which will influence the accuracy of the sound source localization and identification in the sound maps. Therefore, the ground reflections should not be

ignored in the relevant study. And the ground impedance is one of the most important parameters in the study of ground reflection. For this reason, Tam et al. proposed a hybrid method combining the Levenberg–Marquardt (LM) and multiple signal classification (MUSIC) methods to estimate a time-harmonic point sound source location and the ground impedance simultaneously [17, 18]. The MUSIC method is a subspace-based approach of beamforming [19, 20] that makes use of the eigen decomposition of a correlation matrix of all the microphone signals in the frequency domain to separate the signal and noise subspaces. Compared with the traditional delay-and-sum (DAS) and the minimum variance distortionless response (MVDR) beamforming methods [20-22], MUSIC has a higher spatial resolution and lesser sidelobes to achieve a better representation of sound source locations. It has also been adopted in broadband sound source range and bearing estimation [23]. By summing the narrowband MUSIC responses for each frequency bin, the broadband MUSIC (B-MUSIC) response over a frequency range could be implemented to improve the accuracy of localising multiple sound sources in real noisy environments [24]. In order to accurately detect the position of sound sources and ground impedance, the LM method is adopted, which is a modified optimisation process of the Gauss–Newton method by introducing a non-negative damping factor to achieve a reduction in residual vibrations [25-27]. In the work of Tam et al., the Jacobian matrix in the LM optimisation process is performed numerically by the backward finite difference method (FDM). Compared to the Crank Nicolson (CN) method [28], the error produced in the iteration process of backward FDM is usually larger. Nevertheless, with the initial locations from MUSIC, the LM method significantly improves the accuracy of the source locations, and meanwhile provides flexibility to the estimation of ground impedance [17].

Aiming at locating and identifying faults of an uneven surface of a wheel in the wheel/rail system

along with the ground effect, the function of the time-domain kurtosis beamformer is extended to include the fault visualisation and ground impedance estimation simultaneously. To deal with these at the same time, the initial estimation of the fault location is found by using our proposed broadband weighted multiple signal classification (BW-MUSIC) method instead of using the conventional B-MUSIC method. Moreover, the impedance of the reflecting ground surface is found using our proposed modified LM method, which is slightly more efficient than the LM method adopted by the team of Tam et al. Subsequently, the location of a fault on a wheel with an impact noise feature can be accurately determined by the time-domain kurtosis beamformer.

In what follows, Section 2 describes the sound wave model and the theoretical methods in this research. Section 3 and 4 show the corresponding simulation and experimental study and discussions, respectively. At last, the main conclusions are described in Section 5.

2. Methodologies

2.1 Sound wave propagation model influenced by ground effect

Figure 1 shows a sound source propagation model over a flat ground surface with the normal impedance Z [18]. Assuming that p_m is the measured sound pressure, $r_m(x_m, y_m) = \sqrt{(x - x_m)^2 + (y - y_m)^2}$ is the distance between the sound source and the m^{th} receiver microphone, and m is the index of each microphone. $r_i = \sqrt{r_m^2 + 4h_m h_s}$ is the distance between the image source and the m^{th} microphone. The total complex sound pressure at the m^{th} microphone due to the sound source and image source can be expressed as:

$$p_m(r_m) = \frac{\exp(i\omega r_m / c)}{r_m} + Q\frac{\exp(i\omega r_i / c)}{r_i} \tag{1}$$

in which c is the speed of sound, and Q is the complex spherical wave reflection coefficient and can be given by:

$$Q = R_p + (1 - R_p)F(w) \tag{2}$$

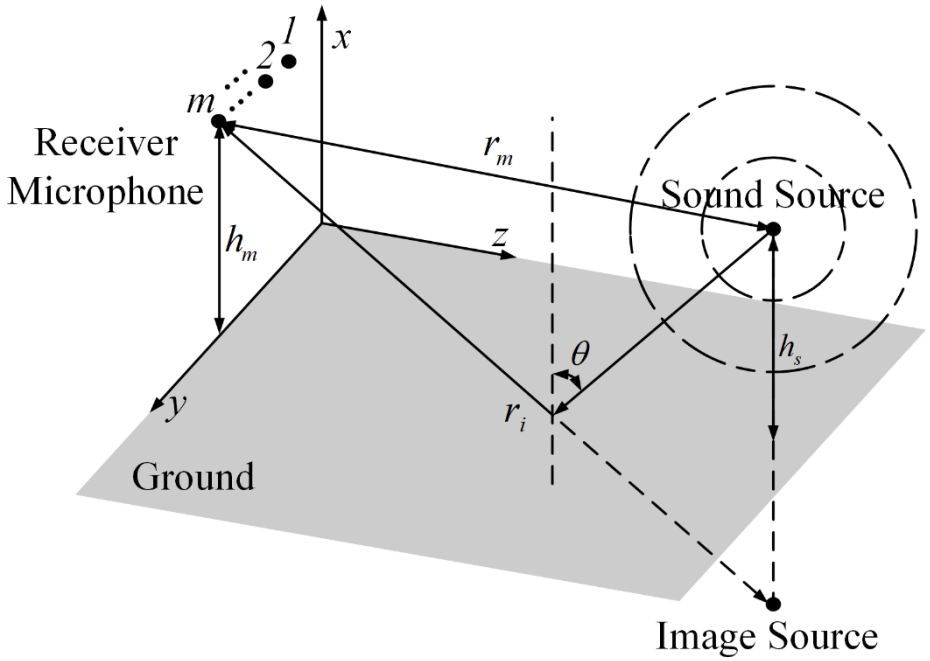

Fig. 1 Sound source propagation model over ground surface.

where R_p is the plane wave reflection coefficient and $F(w)$ is the boundary loss factor. R_p and $F(w)$ can be calculated by the equations below:

$$R_p = (Z\cos\theta - 1)/(Z\cos\theta + 1) \tag{3}$$

$$F(w) = 1 + i\sqrt{\pi}we^{-w^2}\,\mathrm{erfc}(-iw) \tag{4}$$

$$w^2 = (i\omega r_i/2c)[(1/Z) + \cos\theta]^2, \tag{5}$$

in which θ is the incidence angle, $\mathrm{erfc}(\cdot)$ represents the complementary error function and Z is the normal impedance of the ground surface:

$$\begin{aligned} Z &= Z_r + iZ_i \\ &= 0.436\sqrt{\sigma_e/f} + i[0.436\sqrt{\sigma_e/f} + 19.48(\alpha_e/f)] \end{aligned} \tag{6}$$

In this study, the effective rate of change of porosity with depth α_e is assumed to be $150\,m^{-1}$, and the effective flow resistivity at the ground surface σ_e will be estimated by the LM method so that the complex spherical wave reflection coefficient *Q* can be estimated eventually.

2.2 Initial estimation of source location by broadband weighted MUSIC

The MUSIC method is mainly applied in the frequency domain [20]. It makes use of the eigen decomposition of the correlation matrix $\mathbf{R}$ of the measured sound signal to extract the signal and noise subspaces. Because the eigen vectors of the noise subspace $\mathbf{U}_n$ is orthogonal to the basis vectors of the signal subspace $\mathbf{U}_{sn}$, the MUSIC beamforming output can be calculated by the inverse of a scan vector $\mathbf{w}(r_m)$, which belongs to the signal subspace multiplied by the correlation matrix of the noise subspace. By adopting this method, a higher spatial resolution and lesser sidelobes in sound maps can be achieved.

From equation (1), we can assume that the acoustic pressure field measured by microphone array is expressed in vector form as:

$$\mathbf{p}(r_m) = [p_1(r_m) \quad p_2(r_m) \quad \cdots \quad p_M(r_m)] \tag{7}$$

and the measured correlation matrix $\mathbf{R}$ is:

$$\mathbf{R}(r_m) = E[\mathbf{p}(r_m)\mathbf{p}(r_m)^H] \tag{8}$$

which can be expressed as an eigen decomposition form, that is:

$$\mathbf{R} = \mathbf{U}\mathbf{D}\mathbf{U}^H \tag{9}$$

Since the columns of $\mathbf{U}$ are orthogonal, the correlation matrix can be separated into two parts:

$$\begin{aligned} \mathbf{R} &= \mathbf{U}\mathbf{D}\mathbf{U}^H \\ &= \mathbf{U}_{sn}\mathbf{D}_{sn}\mathbf{U}_{sn}^H + \mathbf{U}_n\mathbf{D}_n\mathbf{U}_n^H \end{aligned} \tag{10}$$

where $\mathbf{U}_{sn}$ and $\mathbf{D}_{sn}$ are the eigenvectors and eigenvalues corresponding to the κ largest

eigenvalues of $\mathbf{R}$, $\mathbf{U}_n$, and $\mathbf{D}_n$ are those defined from the remaining eigenvalues from $\kappa+1$ to m. Because $\mathbf{U}_n$ is orthogonal to the basis vectors of the signal subspace, the beamforming power calculated from the correlation matrix consisting of these eigenvectors:

$$\beta_n(r_m) = \mathbf{w}(r_m)^H \mathbf{U}_n \mathbf{U}_n^H \mathbf{w}(r_m), \tag{11}$$

will be minimal for a scan vector $\mathbf{w}(r_m)$ belonging to the signal subspace. The inverse of the beamforming power indicates that the source location has a maximum value when the scan vector $\mathbf{w}(r_m)$ belongs to the signal subspace. The MUSIC beamforming output can be written as:

$$\beta_{MUSIC}(r_m) = \frac{1}{\mathbf{w}(r_m)^H \mathbf{U}_n \mathbf{U}_n^H \mathbf{w}(r_m)} \tag{12}$$

By computing the MUSIC beamforming output $\beta_{MUSIC}(r_m, f)$ for each frequency bin $(1-N)$, the B-MUSIC output can be expressed by averaging these narrowband outputs over a broadband frequency range [23]:

$$\beta_{BM}(r_m) = \frac{1}{N} \sum_{f=f_0}^{f_N} \beta_{MUSIC}(r_m, f) \tag{13}$$

However, as we know, the selection of the computed frequency during narrowband beamforming calculation can be critical. That is because inexact frequency selection would lead to an incorrect localisation result. Considering the different contributions of each frequency in the spectrum, the straightforward summation of the whole frequency range in equation (13) could also lead to an incorrect localisation result. We believe that the estimation of the location of a broadband signal should be weighted by the multiple Fourier transform (FT) results $F(f)$ themselves, so that the interference of the non-dominating frequency band can be eliminated during computation of the beamforming. By such means, The BW-MUSIC output can be given by:

$$\beta_{WBM}(r_m) = \frac{1}{N} \sum_{f=f_0}^{f_N} F(f) \beta_{MUSIC}(r_m, f) \tag{14}$$

This method may be considered a compromise that meets both the broadband and narrowband requirements. In one respect, broadband signal features are considered; on the other hand, the advantage of accurate selection of the dominating frequency during computation of the narrowband beamforming may be retained.

2.3 Further estimation of source location and ground impedance by the LM and Crank Nicolson methods

In this section, the LM optimisation process is introduced to estimate the ground impedance and simultaneously to revise the source location further. An error function of the sound source location (x, y) and the effective flow resistivity at the ground surface σ_e in vector form is defined as [17]:

$$\mathbf{e}(x, y, \sigma_e, \omega) = [\mathbf{S}(x_0, y_0, \sigma_{e_0}, \omega) - \hat{\mathbf{S}}(x, y, \sigma_e, \omega)] \tag{15}$$

in which $\mathbf{S}(x_0, y_0, \sigma_{e_0}, \omega)$ is the initial reference signal vector calculated by beamforming output while $\hat{\mathbf{S}}(x, y, \sigma_e, \omega)$ is the signal vector to be estimated. The objective of the LM optimisation process is to minimise the error function $\mathbf{e}(x, y, \sigma_e, \omega)$. To utilise the LM optimisation process, the Jacobian matrix is introduced and can be calculated by a numerical method:

$$\mathbf{J}(\omega) = [\frac{\partial \mathbf{e}(x, y, \sigma_e, \omega)}{\partial x} \quad \frac{\partial \mathbf{e}(x, y, \sigma_e, \omega)}{\partial y} \quad \frac{\partial \mathbf{e}(x, y, \sigma_e, \omega)}{\partial \sigma_e}], \tag{16}$$

in which the partial differential term $\partial \mathbf{e}(\omega)$ is calculated by the backward FDM in former research:

$$\frac{\partial \mathbf{e}(\omega)}{\partial x} = \frac{\mathbf{e}(x) - \mathbf{e}(x - \Delta x)}{\Delta x} \tag{17}$$

which will be replaced by the Crank Nicolson method:

$$\frac{\partial \mathbf{e}(\omega)}{\partial x} = \frac{\mathbf{e}(x + \Delta x) - \mathbf{e}(x - \Delta x)}{2\Delta x} \tag{18}$$

in this study, which yields a more accurate approximation. The comparison of these two FDMs is presented in Section 3.1. The variable intervals in Eq. 18 are set to $\Delta x = \Delta y = 10^{-13}$ m and

$\Delta\sigma_e$=100 MKS rayls/m . The $(n+1)^{\text{th}}$ iteration result ξ_{n+1} of the LM optimisation process is:

$$\xi_{n+1} = \xi_n - \{\mathbf{J}(\omega)^T \mathbf{J}(\omega) + \lambda \text{diag}[\mathbf{J}(\omega)^T \mathbf{J}(\omega)]\}^{-1} \mathbf{J}(\omega)^T \mathbf{e}(\omega) ,$$

(19)

in which λ is a positive scalar regularisation parameter. This parameter is introduced to overcome the difficulty when $\mathbf{J}(\omega)^T \mathbf{e}(\omega)$ is singular or nearly singular. When $\lambda = 0$ the optimisation process becomes the well-known Gauss-Newton optimisation method. Y. He et al. presents a corrected LM algorithm to adjust the value of λ so that the whole process is more efficient and robust. In this study, λ is set at 0.01 to meet the stability demand of estimation.

2.4 Fault detection by time-domain kurtosis beamforming

Time-domain beamforming output can be represented using the peak value, root mean square (RMS) value, and kurtosis. Among these three estimators, kurtosis is considered the best indicator of signal impulsiveness for fault detection. Kurtosis is the fourth standardised moment, which is defined as

$$Kurt(x) = \frac{E\{[x - \mu(x)]^4\}}{[\sigma(x)]^4} \tag{20}$$

in which $\mu(x)$ is the mean value of x, $\sigma(x)$ is the standard deviation of x, and E represents the expected value of the quantity. The kurtosis beamforming output is:

$$Kurt(r_m) = \frac{E\left(\left\{b(r_m,t) - \mu\left[b(r_m,t)\right]\right\}^4\right)}{\left\{\sigma\left[b(r_m,t)\right]\right\}^4} , \tag{21}$$

in which $b(r_m,t)$ is the time-domain DAS beamforming output in the near-field assumption:

$$b(r_m,t) = \frac{1}{M}\sum_{m=1}^{M} p_m(t - \frac{r_m}{c}) , \tag{22}$$

where c is the representative speed of sound. Because the time-domain DAS beamforming output $b(r_m,t)$ is a function of time and space, it can emphasise the temporal characteristics of the source signal [14].

3. Simulation

3.1 LM estimation process by using the backward finite difference and CN methods

Numerical simulations are performed by MATLAB to compare the performance of the LM method by adopting the backward finite difference and CN methods during the calculation of the Jacobian matrix. The sound source location is assumed at (0.5 m, 1 m), while the effective flow resistivity is assumed to be 200,000 MKS rayls/m. Once the effective flow resistivity is estimated, the value of the normal impedance of the ground surface can be easily derived from equation (6). The frequency of the sound source is set to be 1,000 Hz throughout the analysis. To conduct the LM optimisation estimation process, an initial input localisation from beamforming is assumed at (0.55 m, 1.05 m), and the preliminary estimation of the effective flow resistivity is assumed to be 220,000 MKS rayls/m, which is typical for sandy ground. The details of LM and LM–CN estimation theories are introduced in Section 2.3. The comparison of the LM method is shown in Fig. 2 as a dashed line for backward finite difference in and a solid line for LM–CN. The iterations are computed up to 10,000 times in both processes so that the estimated parameters converge on the actual values as far as possible. Figures 2(a) and 2(b) show the estimated coordinates of the sound source, and Fig. 2(c) shows the estimated effective flow resistivity. Clearly by replacing the backward FDM with the CN method, the rate of convergence among all three sets is improved. The initial values along the solid lines move towards the actual values more quickly than the dashed lines. Furthermore, the convergence values by

the LM–CN method are closer to the actual values.

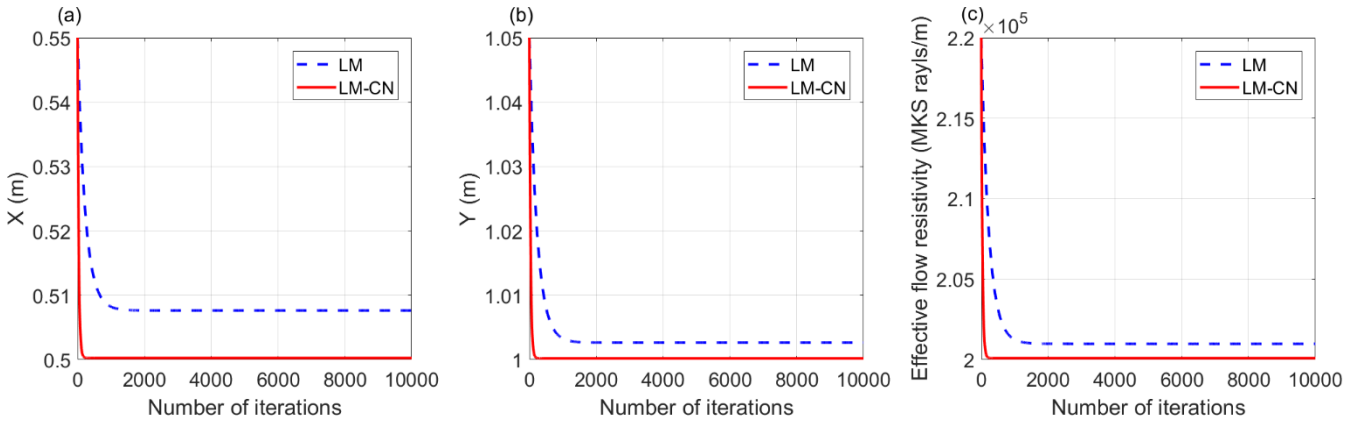

Fig. 2 Comparison of simulation results of the Levenberg–Marquardt method using the backward finite difference and Crank Nicolson methods.

3.2 Initial localisation results simulation

Localisation simulations are performed by the finite element method (FEM) software COMSOL to investigate the performance of the proposed BW-MUSIC method against the traditional DAS and MUSIC method, under the influence of ground effect. The transient pressure acoustics model was adopted in the simulations and a Gaussian pulse was set at the point source to imitate an impulsive signal. The scalar wave equation of the transient pressure acoustics model is:

$$\frac{1}{\rho c^2}\frac{\partial p_t}{\partial t^2}+\nabla\cdot\left[-\frac{1}{\rho}\left(\nabla p_t-\mathbf{q}_d\right)\right]=Q_m \tag{23}$$

The wave equation of the Gaussian pulse source is:

$$\frac{1}{\rho c^2}\frac{\partial p_t}{\partial t^2}+\nabla\cdot\left[-\frac{1}{\rho}\left(\nabla p_t-\mathbf{q}_d\right)\right]=\frac{4\pi}{\rho c}S\delta(\mathbf{x}-\mathbf{x}_0)\ , \tag{24}$$

in which p_t is the total acoustic pressure, ρ is the fluid density, $\mathbf{q}_d$ is the dipole domain source, Q_m is the monopole domain source, and S is the source strength:

$$S = -A_m \rho \frac{\pi}{2} f_0^2 (t - t_p) e^{-\pi^2 f_0^2 (t - t_p)^2} \quad , \tag{25}$$

where A_m is the value of the pulse amplitude, f_0 is the frequency bandwidth, and t_p is the pulse peak time. To simulate the ground impedance, an impedance boundary condition under the sound area was set while the other three sides of the sound area were surrounded by a perfectly matched layer (PML). The impedance boundary condition is the following:

$$-\mathbf{n} \cdot \left[-\frac{1}{\rho_c} (\nabla p - \mathbf{q}_d) \right] = \frac{1}{Z_a} \frac{\partial p_t}{\partial t} \quad , \tag{26}$$

in which the acoustic input impedance Z_a is related to the acoustic impedance Z_{ac} and the mechanical impedance Z_{mech} via the area A of the boundary:

$$Z_{mech} = A Z_a = A^2 Z_{ac} \tag{27}$$

The point source location was at (2.8 m, 3.5 m) and a simulative uniform linear microphone array was adopted. The whole geometry of the simulation is shown in Fig. 3.

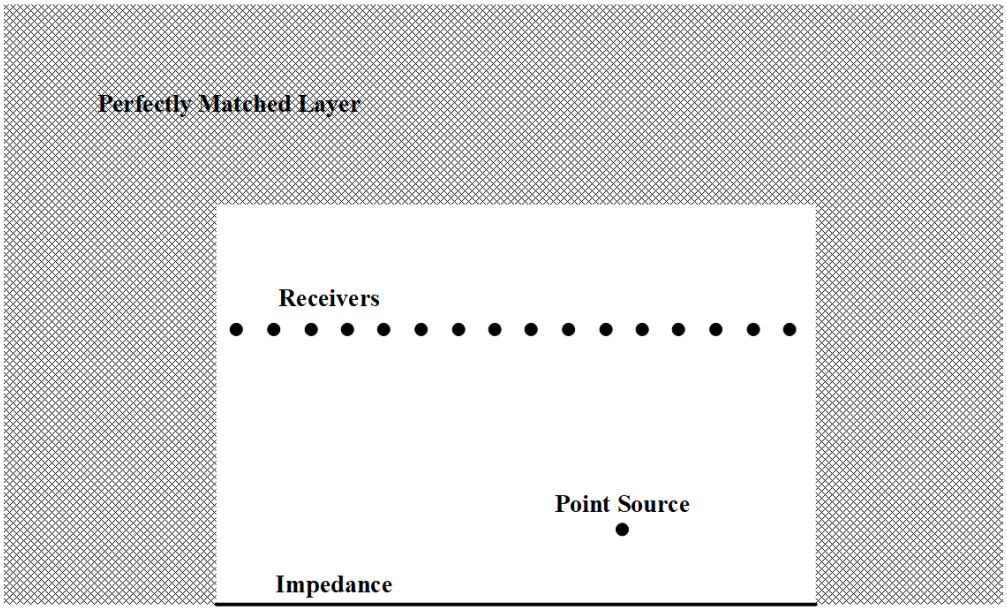

Fig. 3 Geometry of the simulation by COMSOL.

Figure 4 shows the simulated localisation results obtained using the DAS, MUSIC, weighted

broadband DAS, and weighted broadband MUSIC methods. Because the impedance domain was active under the sound area, in Fig. 4(1a) and (1b) the sidelobes and the main lobe in the sound map are hardly distinguishable. The performance of the conventional DAS and MUSIC could be severely disrupted by the reflection effect. Comparing these two plots, the mentioned condition is slightly improved in Fig. 4(1b) because the MUSIC method is credited with a higher spatial resolution and lesser sidelobes. Figure 4(2a) shows the localisation result of weighted broadband DAS. The sidelobes in this plot are much lesser, yet the spatial resolution is still low, and the point source at (2.8 m, 3.5 m) and its image source at (2.8 m, 2.5 m) due to the impedance combine into one main lobe. The aforementioned problems are perfectly solved in Fig. 4 (2b) by BW-MUSIC. The localisation result is quite accurate, and nearly no sidelobe distortion may be noticed in the sound map.

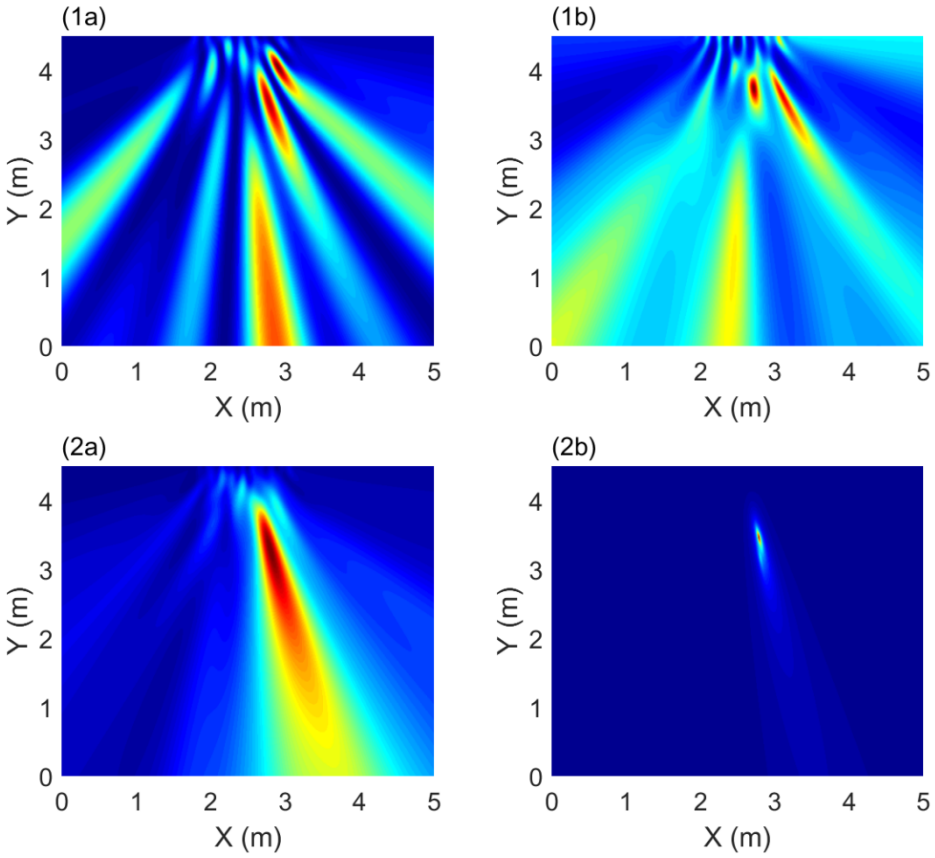

Fig. 4 Localisation results from DAS (1a), MUSIC (1b), weighted broadband DAS (2a), and

weighted broadband MUSIC (2b).

4. Experimental study

4.1 The roller test rig and testing wheels

To simulate an actual wheel/rail system, a roller test rig was designed and constructed as shown in Fig. 5, which is composed of two rollers and two different shafts. One shaft is coupled with a larger cast iron wheel, which serves as the imitating rail by pulley, and the other shaft is coupled with a smaller cast iron wheel, which serves as the testing wheel. Both shafts were driven by 60 W/220 V direct current (DC) motors (5IK60RGU-CF) with decelerators (5GU-3K). Universal coupling was applied to ensure that the motion of the testing wheel including undergoing a fault possessed enough space. The different speeds of the two shafts are achieved by the optical tachometers.

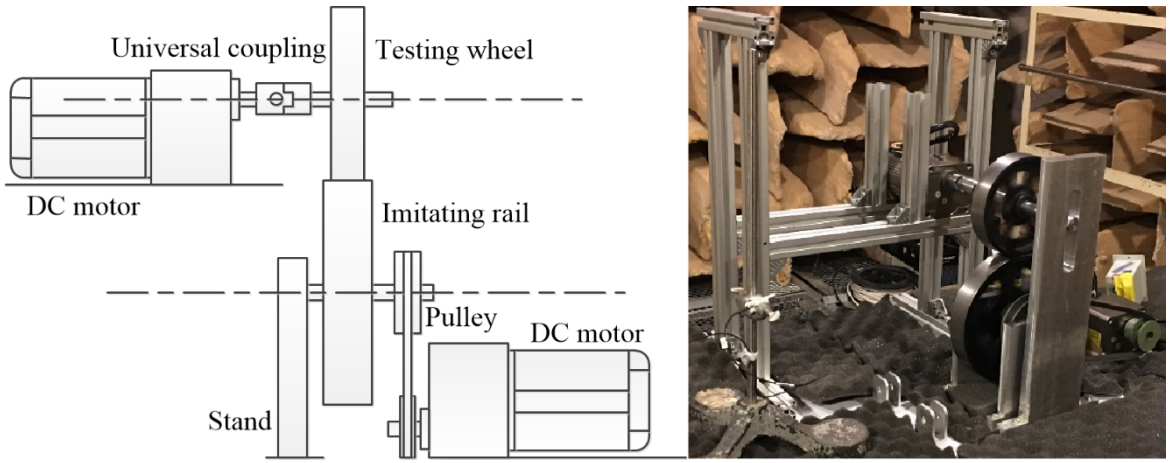

Fig. 5 Sketch and snapshot of the roller test rig.

The defect location is considered as the faulty wheel location in this paper. Our purpose is to localize and to identify the faulty wheel from other adjacent pristine wheels of the moving train. The snapshots and corresponding rolling time-variant acoustic signals of healthy and faulty wheels are shown in Fig. 6. The size of defect on the wheel surface is discussed in the former research [14], and

it is very close to the real defects. Figure 6 (1a) shows a snapshot of a healthy wheel. No apparent damage can be discovered on the wheel surface. However, in Fig. 6 (2a), the faults on the wheel surface are extremely severe, as marked in red in the snapshot. As a result, compared with the signal in Fig. 6 (1b), the impulsiveness of the signal in Fig. 6 (2b) is obvious. To distinguish the healthy and faulty wheels, the kurtosis value is applied to reflect the impulsiveness of the signal.

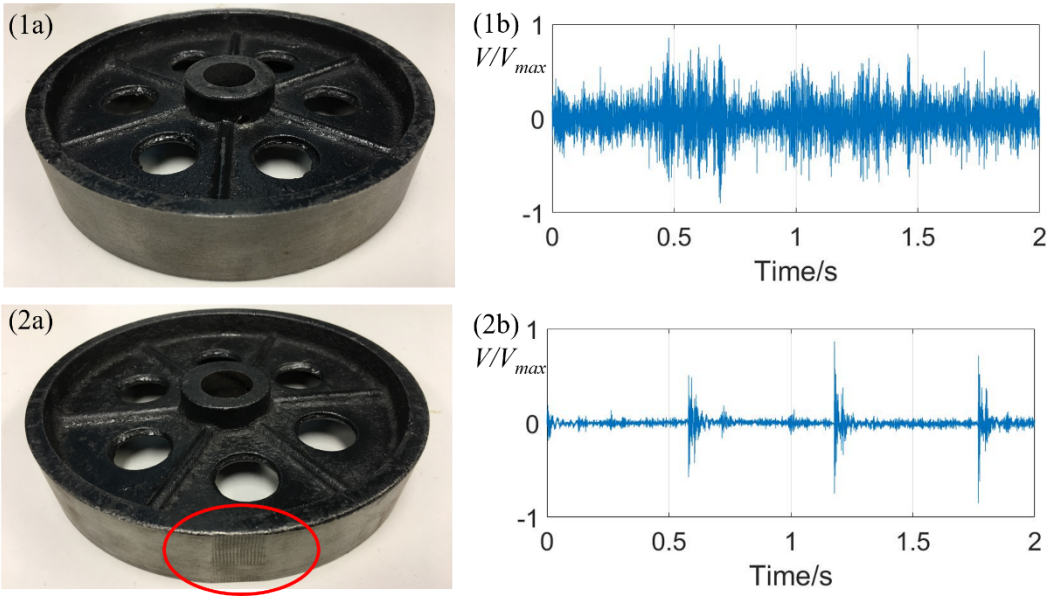

Fig. 6 Sketch and time-domain signals of healthy and faulty wheels. (1a) snapshot of the healthy wheel, (1b) time-domain signal of the healthy wheel; (2a) snapshot of the faulty wheel; (2b) time-domain signal of the faulty wheel.

4.2 Initial localisation results from broadband weighted MUSIC

As the simulation comparison results of B-MUSIC and BW-MUSIC show, the sound map which is not weighted by the multiple FT results can be distorted by the superposition of the sidelobes. Experimental testing is conducted to compare these two methods. All experiments were performed in a semi-anechoic chamber with a background noise level of less than 15 dBA, and a cut-off frequency of 80 Hz to avoid sound reflections from the surrounding walls and ceiling. In particular, the original

wire gauze floor of the anechoic chamber is covered by timber sheeting to achieve the sound wave propagation model with ground effect. Figure 7 shows the experimental setup consisting two roller test rigs, a 32-channel quadrate microphone array, two Brüel & Kjær Type 2694-A 16-channel DeltaTron conditioning amplifiers, eight NI 9234 four-channel data acquisition cards, and a desktop computer.

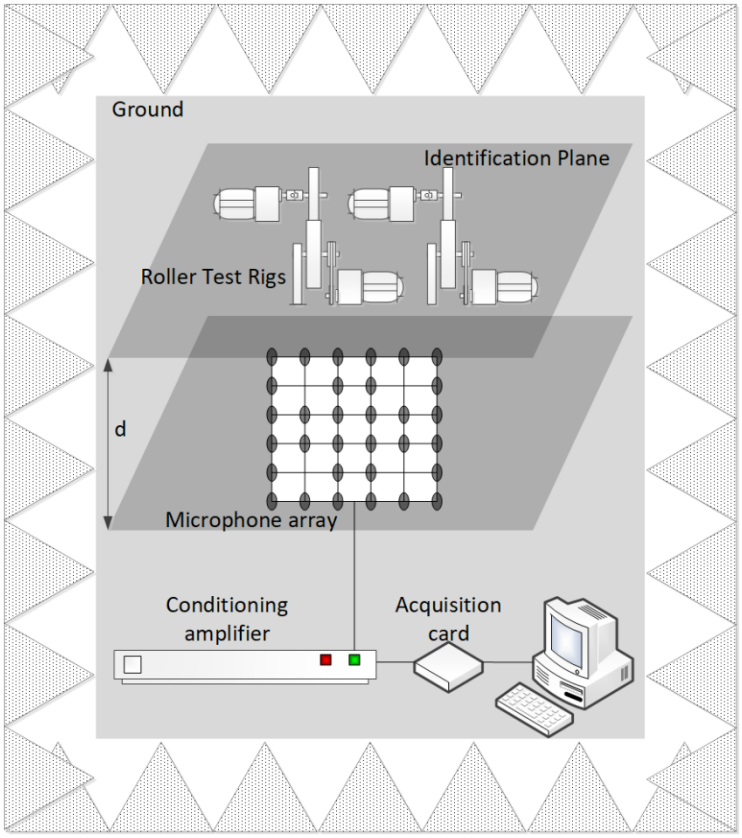

Fig. 7 Experimental setup.

In the localisation results that are shown in Fig. 8, two random noise sound sources tagged as □ and ○ are installed in the identification plane. The x-axis is set as the ground surface so that the fourth quadrant in the sound map indicates the localisation of image sources, which are tagged as ◇ and X. Figure 8(a) shows the localisation results of B-MUSIC while Fig. 8(b) shows the localisation results of BW-MUSIC. Due to the difference in volume of the two sound sources, the beamformer output at

□ is significantly higher than ○. In Fig. 8(a) a bulk of superposition of sidelobes around the sound sources can be easily noticed in consequence of the ground effect. The image sources and sound sources are mixed together in this sound map. The challenge is noticeably improved in Fig. 8(b). With the weighting by the multiple FT results, the beamformer outputs at sound source locations are enhanced. The image sources are separated from the sound sources with a much weaker sound power in the fourth quadrant.

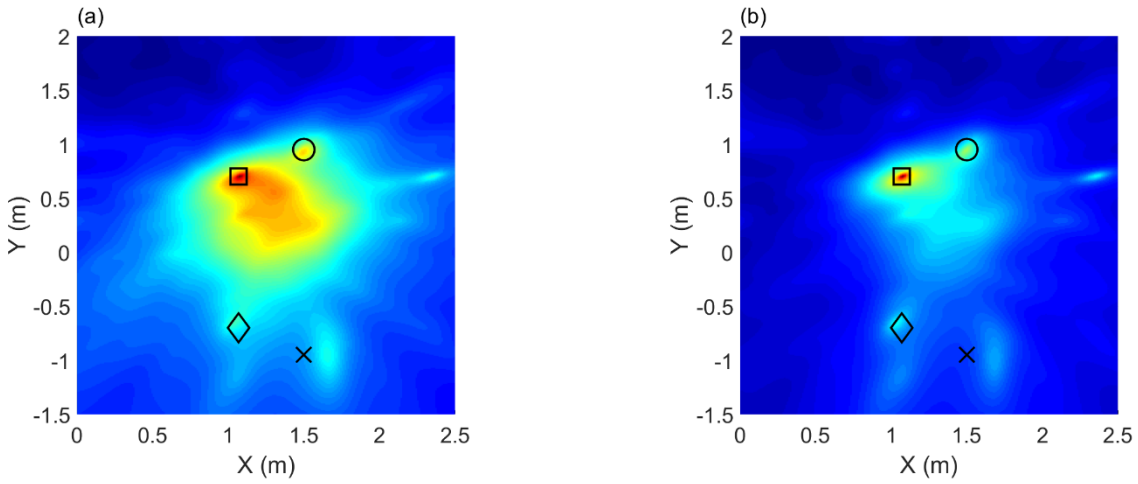

Fig. 8 Localisation results from broadband MUSIC and weighted broadband MUSIC (□ and ○: location of sound sources, ◇ and X: location of image sources). (a) broadband MUSIC localisation result, (b) weighted broadband MUSIC localisation result.

4.3 Fault detection results from kurtosis beamforming

In this section the random noise sound sources in Fig. 8 are replaced by two roller test rigs with healthy and faulty wheels. Figure 9 shows the fault detection and localisation results by comparing the B-MUSIC, BW-MUSIC, time-domain DAS beamforming, and kurtosis beamforming methods. The x-axis in Fig. 9 is also set as the ground surface. Consistently, in Fig. 9, the healthy and faulty wheels are tagged as □ and ○, respectively, and the corresponding image sources are tagged as ◇ and X.

In this case, the performance of the B-MUSIC and BW-MUSIC methods is nearly the same. The influence of the superposition of sidelobes in Fig. 9(1a) is not remarkable compared with the sound map in Fig. 9(1b). In order to highlight the ability of the fault detection of kurtosis beamforming method, the sound volume of the roller test rig with the healthy wheel is set louder. Therefore, the amplitude of the beamforming output at □ is appreciably higher than ○ in Fig. 9(1a) and (1b).

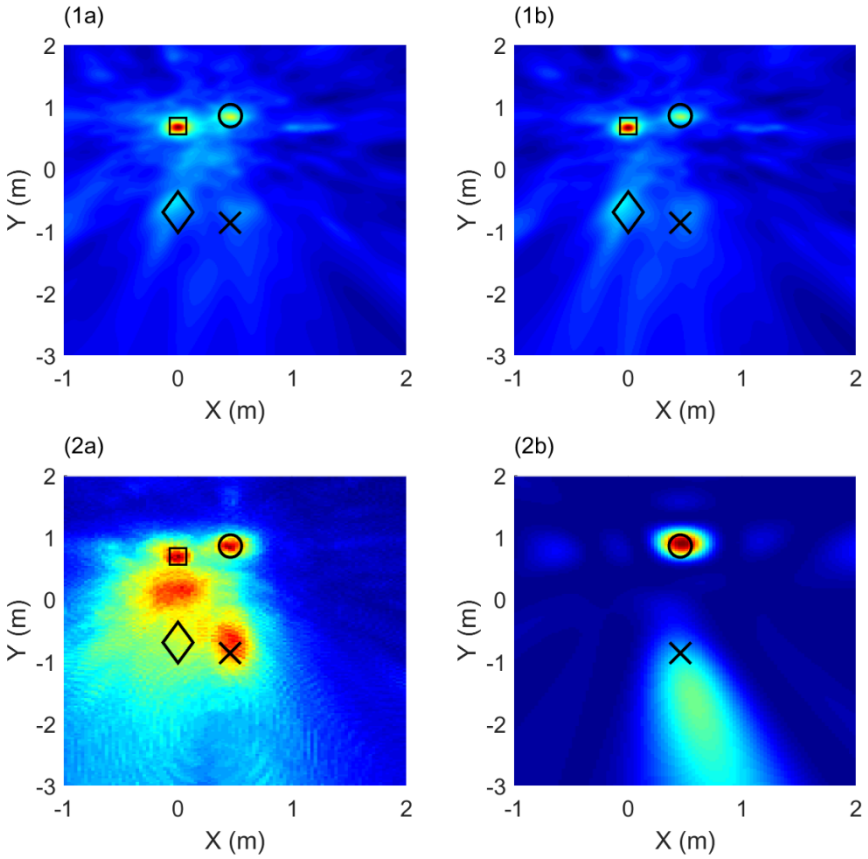

Fig. 9 Fault detection and localisation results for a healthy wheel and a faulty wheel (□: location of the healthy wheel, ○: location of the faulty wheel, ◇ and X: location of image sources). (1a) broadband MUSIC localisation result, (1b) weighted broadband MUSIC localisation result, (2a) time-domain DAS beamforming result, (2b) kurtosis beamforming result.

Table 1 shows the percentage error in both the x and y-directions of fault detection and localisation by different methods, which is defined as the ratio between the error and the actual fault

location in percentage:

$$\delta_x = 100\% \times \left| \frac{x_a - x_e}{x_a} \right| \tag{28}$$

$$\delta_y = 100\% \times \left| \frac{y_a - y_e}{y_a} \right| , \tag{29}$$

in which x_a and y_a are the actual fault coordinates, while x_e and y_e are the estimated coordinates by the beamforming approach. For the B-MUSIC, BW-MUSIC, and DAS method, due to the interference of the healthy wheel, the percentage error is quite large. Nevertheless, in accordance with the fault detection results shown in Fig. 9, the kurtosis beamforming method provides smaller error. The fault detection and localisation results are observed to be accurate.

Table 1

Percentage error of fault detection and localisation by different methods

Localisation method	x-direction	y-direction
B-MUSIC	100.00%	24.14%
BW-MUSIC	100.00%	24.14%
DAS	102.08%	20.69%
Kurtosis beamforming	2.08%	3.45%

4.4 Ground impedance estimation results from the Levenberg–Marquardt and Crank Nicolson method

As mentioned in Sections 2.3 and 3.1, the LM–CN method is a better parameter estimation

approach than the LM method for ground impedance estimation. With the results from BW-MUSIC as the initial inputs of the source location, the LM–CN method is performed in this section of the study. The estimation in the real and imaginary part of normal ground impedance from 500 to 6,000 Hz in the former experiment is shown in Fig. 10. The real part of the normal impedance ranges from 0.93 to 0.99, while the imaginary part ranges from -0.03 to 0.11. Because the image source was expected to be considerable in this study, a hard timber sheeting covered with paint was employed as the imitation of the ground, and the estimated ground impedance in the experiment was extremely high. The accuracy of the estimation results was confirmed in the following.

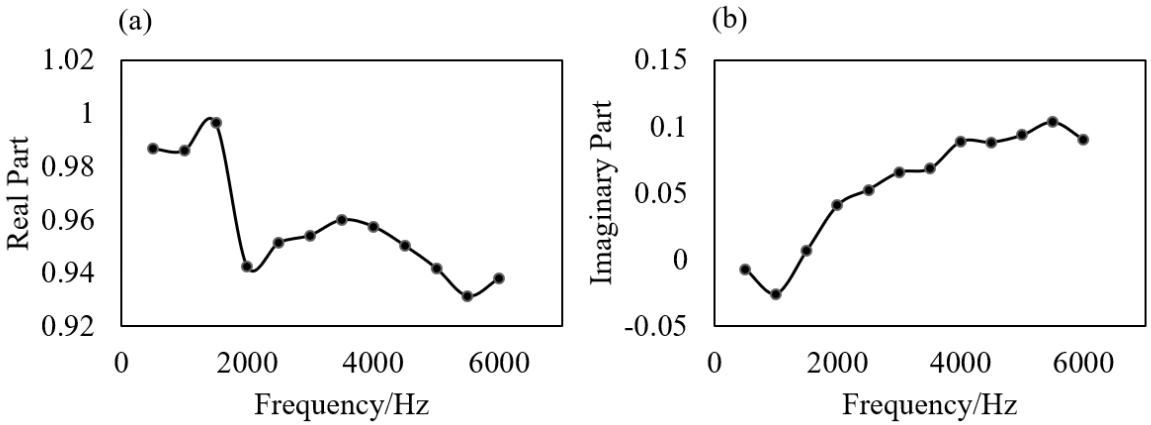

Fig. 10 Normal impedance of ground surface estimation by the LM–CN method. (a) real part, (b) imaginary part.

Figure 11 shows the percentage error of normal impedance estimation in both the real and imaginary part. In Fig. 11(a), the fluctuation of errors from 500 to 6,000 Hz is very slight. The largest percentage error (5.31%) occurs at 1,500 Hz. The performance of normal impedance real part estimation is quite acceptable. However, in Fig. 11(b), the largest percentage error increases to 108.30%. The percentage error of one-third of the estimation results in impedance in the imaginary part is larger than 24%, especially in the low frequency range. Referring to the estimation results in

Fig. 10(b), in the low frequency range from 500 to 1,500 Hz, the value of the imaginary part is very close to 0. This could be the reason why the percentage error is quite large. In this range, small deviations could lead to a large error.

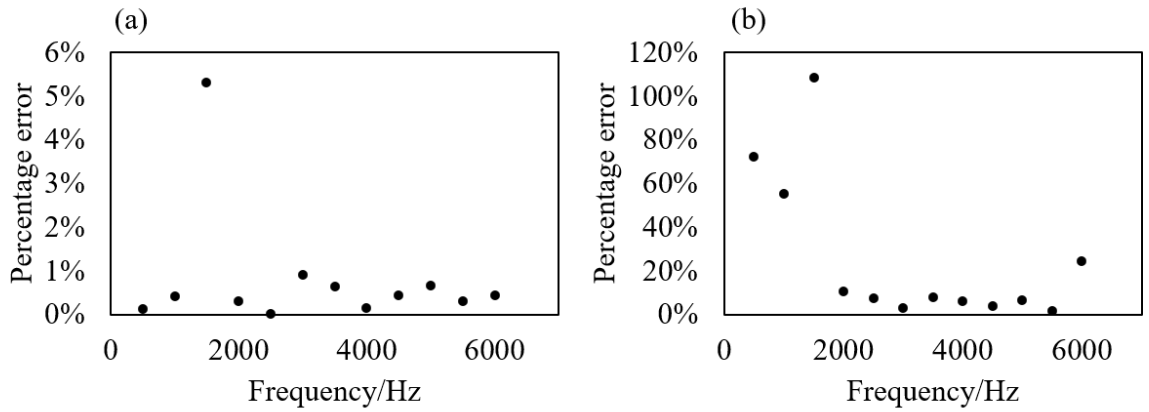

Fig. 11 Percentage error of normal impedance estimation. (a) real part, (b) imaginary part.

5. Conclusion

The objective of this study is to propose a hybrid microphone array signal processing approach for faulty wheel identification and ground impedance estimation. Its performance was compared with the previous LM and MUSIC method by simulation and experimental study. The major conclusions are as follows:

1. Numerical simulations and experimental study have both been adopted to locate the sound source using the BW-MUSIC method. Compared with the MUSIC and B-MUSIC methods, performance with ground reflection and broadband signals is much better. In the simulation by FEM, with the interference of imitative ground reflection, the localisation result by BW-MUSIC was more accurate than other methods. The range of the main lobe was smaller, with nearly no sidelobe distortion. Consistent results were achieved in the experimental study. With multiple sound sources and ground reflection, the BW-MUSIC method provided a

separate and distinct localisation result in the sound map compared with B-MUSIC.

2. Typically, time-domain beamforming can yield accurate positions of the sound sources in a field of multiple sound sources based on acoustical power. In the experiment adopting the impact noise generated by faulty wheels, the kurtosis beamforming outperforms the time-domain DAS and BW-MUSIC methods to extract the features of impulsive signals. The impact noise source can be detected accurately. Consistently, the kurtosis beamforming method provides smaller errors.
3. In numerical simulation by MATLAB, the impedance of the reflecting ground surface can be estimated by the LM–CN method. Compared with the former LM approach to estimate ground impedance, the LM–CN method provides a preferable convergence path. The rate of convergence among all parameters is improved. The convergence values by LM–CN method are closer to the actual values than the LM method. In the experimental study, the estimation results and their accuracy in the real and imaginary part of normal ground impedance from 500 to 6,000 Hz is shown.

Acknowledgements

The study is supported and funded by the General Research Grant from the Hong Kong SAR government (PolyU 5140/13E) and the Hong Kong Polytechnic University (Grant No: G-YBDL).

References

[1] Vér I, Ventres C, Myles M. Wheel/rail noise—part III: impact noise generation by wheel and rail discontinuities. J Sound Vib. 1976;46:395-417.

[2] Wang Y, Liang M. An adaptive SK technique and its application for fault detection of rolling element bearings. Mech Syst Sig Process. 2011;25:1750-64.

[3] Alemi A, Corman F, Lodewijks G. Condition monitoring approaches for the detection of railway wheel defects. 2017;231:961-81.

[4] Su Z, Ye L, Lu Y. Guided Lamb waves for identification of damage in composite structures: A review. J Sound Vib. 2006;295:753-80.

[5] Peng Z, Kessissoglou N. An integrated approach to fault diagnosis of machinery using wear debris and vibration analysis. Wear. 2003;255:1221-32.

[6] Dornfeld D, Cai HG. An investigation of grinding and wheel loading using acoustic emission. J Eng Ind. 1984;106:28-33.

[7] Beebe RS. Machine Condition Monitoring: How to Predict Maintenance Requirements for Rotating and Stationary Plant: MCM Consultants; 1995.

[8] Matsumoto A, Sato Y, Ohno H, Tomeoka M, Matsumoto K, Kurihara J, et al. A new measuring method of wheel–rail contact forces and related considerations. Wear. 2008;265:1518-25.

[9] Barke D, Chiu W. Structural health monitoring in the railway industry: a review. Struct Health Monit. 2005;4:81-93.

[10] Drinkwater BW, Wilcox PD. Ultrasonic arrays for non-destructive evaluation: A review. NDT E Int. 2006;39:525-41.

[11] Shibata K, Takahashi A, Shirai T. Fault diagnosis of rotating machinery through visualisation of sound signals. Mech Syst Sig Process. 2000;14:229-41.

[12] Lu W, Jiang W, Yuan G, Yan L. A gearbox fault diagnosis scheme based on near-field acoustic holography and spatial distribution features of sound field. J Sound Vib. 2013;332:2593-610.

[13] Cabada EC, Leclere Q, Antoni J, Hamzaoui N. Fault detection in rotating machines with beamforming: Spatial visualization of diagnosis features. Mech Syst Sig Process. 2017;97:33-43.

[14] Chen L, Choy YS, Wang TG, Chiang YK. Fault detection of wheel in wheel/rail system using kurtosis beamforming method. Struct Health Monit. 2019:1475921719855444.

[15] Wang Y, Xiang J, Markert R, Liang M. Spectral kurtosis for fault detection, diagnosis and prognostics of rotating machines: A review with applications. Mech Syst Sig Process. 2016;66:679-98.

[16] Antoni J. The spectral kurtosis: a useful tool for characterising non-stationary signals. Mech Syst Sig Process. 2006;20:282-307.

[17] Tam K-C, Lau S-K, Tang S-K. Estimation of source location and ground impedance using a hybrid multiple signal classification and Levenberg–Marquardt approach. J Sound Vib. 2016;374:279-96.

[18] Li K, Attenborough K, Heap N. Source height determination by ground effect inversion in the presence of a sound velocity gradient. J Sound Vib. 1991;145:111-28.

[19] Schmidt R. Multiple emitter location and signal parameter estimation. IEEE Trans Antennas Propag. 1986;34:276-80.

[20] Kim Y-H, Choi J-W. Sound visualization and manipulation: John Wiley & Sons; 2013.

[21] Cigada A, Ripamonti F, Vanali M. The delay & sum algorithm applied to microphone array measurements: numerical analysis and experimental validation. Mech Syst Sig Process. 2007;21:2645-64.

[22] Li J, Stoica P, Wang Z. On robust Capon beamforming and diagonal loading. IEEE Trans Signal Process. 2003;51:1702-15.

[23] Jeffers R, Bell KL, Van Trees HL. Broadband passive range estimation using MUSIC. 2002 IEEE International Conference on Acoustics, Speech, and Signal Processing: IEEE; 2002. p. III-2921-III-4.

[24] Ishi CT, Chatot O, Ishiguro H, Hagita N. Evaluation of a MUSIC-based real-time sound localization of multiple sound sources in real noisy environments. 2009 IEEE/RSJ International Conference on Intelligent Robots and Systems: IEEE; 2009. p. 2027-32.

[25] Marquardt DW. An algorithm for least-squares estimation of nonlinear parameters. Journal of the society for Industrial and Applied Mathematics. 1963;11:431-41.

[26] Levenberg K. A method for the solution of certain non-linear problems in least squares. Q Appl Math. 1944;2:164-8.

[27] Hartley HO. The modified Gauss-Newton method for the fitting of non-linear regression functions by least squares. Technometrics. 1961;3:269-80.

[28] Sweilam N, Khader M, Mahdy A. Crank-Nicolson finite difference method for solving time-fractional diffusion equation. Journal of Fractional Calculus and Applications. 2012;2:1-9.